Research Square

Preprints are preliminary reports that have not undergone peer review.
They should not be considered conclusive, used to inform clinical practice,
or referenced by the media as validated information.

A spin-crossover route to charge ordering in Fe_4O_5

Xiang Li

xiang.li@esrf.fr

European Synchrotron Radiation Facility https://orcid.org/0000-0003-3259-1784

Denis Vasiukov

Division of Synchrotron Radiation Research, Lund University

Maxim Bykov

Goethe University Frankfurt https://orcid.org/0000-0003-0248-1728

Susanne Müller

European Synchrotron Radiation Facility

Anthony Lanati

Macquarie University https://orcid.org/0000-0002-3317-5697

Efim Kolesnikov

Institute for Mineralogy, University of Münster

Georgios Aprilis

European Synchrotron Radiation Facility

Elena Bykova

Institute of Geosciences, University Frankfurt

Hu Tang

Jilin University https://orcid.org/0000-0003-1571-8843

Paul Pangritz

Institute for Mineralogy, University of Münster

Arno Rohrbach

Institute for Mineralogy, University of Münster https://orcid.org/0000-0003-2668-6883

Sergey Yaroslavtsev

European Synchrotron Radiation Facility

Ekaterina Klyushina

Department of Physics, Lund University https://orcid.org/0009-0005-1548-329X

Oskar Stepancic

Department of Physics, Lund University https://orcid.org/0009-0004-4553-3422

Aleksandr Chumakov

ESRF-The European Synchrotron https://orcid.org/0000-0002-0755-0422

Davide Comboni

European Synchrotron Radiation Facility

Michael Hanfland
European Synchrotron Radiation Facility
Stephan Klemme
Institute for Mineralogy, University of Münster https://orcid.org/0000-0001-7859-9779
Elizabeth Blackburn
Lund University https://orcid.org/0000-0002-5119-6053
Leonid Dubrovinsky
Bayerisches Geoinstitut https://orcid.org/0000-0002-3717-7585
Carmen Sanchez-Valle
Institute for Mineralogy, University of Münster https://orcid.org/0000-0001-5046-1612
Ilya Kupenko
European Synchrotron Radiation Facility

Article

Keywords:

Posted Date: November 3rd, 2026

DOI: https://doi.org/10.21203/rs.3.rs-11443065/v1

License: This work is licensed under a Creative Commons Attribution 4.0 International License.
Read Full License

Additional Declarations: There is **NO** Competing Interest.

Abstract

Charge order reflects a delicate balance between localization and itinerancy, yet the microscopic parameters that control this balance remain poorly understood. Here we identify spin crossover as a route to control charge order in mixed-valence Fe_4O_5. Using single-crystal X-ray diffraction and synchrotron Mössbauer source spectroscopy to 112 GPa at room temperature, we reveal three previously unreported charge-ordered phases associated with two site-selective spin crossovers. The first two phases are characterized by Fe-Fe dimers, whereas the highest-pressure phase hosts isolated planar bent Fe trimers, a motif not previously reported in iron oxides. All three charge-ordered phases are confined to mixed spin state regimes: charge order emerges as an octahedral Fe site enters spin crossover, persists while high-spin and low-spin states coexist on that site, and vanishes once the crossover is complete. Between the two spin crossovers, a charge-disordered phase in which high-spin and low-spin iron occupy different sites shows that spin-state heterogeneity within a single site is required for ordering. We propose that near spin-state degeneracy, enhanced charge-lattice coupling favours localization and stabilizes charge order. Our results establish spin crossover as an externally tunable route to stabilizing and controlling charge order in mixed-valence materials.

Main

Transition-metal compounds often host strongly intertwined charge, orbital and spin degrees of freedom, giving rise to diverse collective electronic and magnetic states[1–5]. Charge ordering is a prominent manifestation of this interplay, involving the spatial differentiation of electronic charge among otherwise equivalent crystallographic sites. A paradigmatic example is magnetite, where the Verwey transition couples charge ordering to a metal-insulator transition and stabilizes linear three-iron trimerons through shortened Fe-Fe bonds[1,3]. Charge-ordering transitions have since been identified in a broad range of mixed-valence transition-metal compounds, including iron oxides[3,6–8], manganites[9] and cobaltites[10], where charge localization can profoundly reshape electronic, structural, magnetic and ferroic properties. Understanding the microscopic factors that stabilize charge order, and how it can be tuned by external parameters, is therefore essential for controlling these emergent properties.

One potential microscopic handle on charge order is the spin state, which can be tuned by pressure[4,11–13], temperature[14] or light[15]. Within a spin crossover, high-spin and low-spin states can coexist on the same crystallographic site and may order into spin-state superstructures[14,16–18]. Their distinct ionic sizes, orbital occupancies and local bonding create strong local heterogeneity, while electronic and elastic interactions near spin-state degeneracy can further favour symmetry breaking[16]. In a mixed-valence system, these effects may shift the balance between charge localization and itinerancy, raising the possibility that spin crossover itself can stabilize and control charge order.

Fe_4O_5 is expected to be a good model system to test this possibility. It combines mixed-valence iron distributed over one trigonal-prismatic and two crystallographically distinct octahedral sites[19], several

well-separated site-selective spin crossovers[20–22], and a rich charge-ordering phase diagram[7,23]. At low temperature and ambient pressure, charge ordering produces incommensurate superstructure with competing Fe-Fe dimers and linear trimers in the octahedral chains[7], with compression increasing the ordering temperature and modifying the ordering patterns[23]. At room temperature, by contrast, no symmetry lowering was detected up to ~ 100 GPa, and the transitions reported near 50 and 84 GPa were attributed to spin crossovers within the parent structure, the latter accompanied by metallization[21].

Here we show that spin crossover provides a route to control charge order. At room temperature, compression induces charge order in Fe_4O_5 in two separate episodes, each occurring while one of its octahedral sites undergoes spin crossover. Using single-crystal X-ray diffraction and synchrotron Mössbauer source spectroscopy to 112 GPa, we identify three charge-ordered phases, two in the first episode and one in the second, separated by a charge-disordered phase (Fig. 1a). The last of the charge ordered phases abandons the linear Fe-Fe motifs found in other charge-ordered iron oxides, including the trimerons of magnetite[3], in favour of bent trimers. Each episode ends as soon as the corresponding crossover is complete, and charge order is absent where high-spin and low-spin iron coexist on different sites. These observations show that spin-state heterogeneity within a single octahedral site is a key condition for charge ordering. We propose that spin crossover enhances the charge-lattice coupling near spin-state degeneracy, favouring charge localization within the mixed-spin regime. This route to charge order may extend beyond compression.

Sequence of pressure-induced phase transitions

At ambient conditions, Fe_4O_5 adopts an orthorhombic *Cmcm* structure (no. 63) as reported previously[19,21,23]. This phase (Supplementary Data 1) persists up to 38(1) GPa above which some Bragg reflections split, signaling the emergence of a new high-pressure phase coexisting with the parent *Cmcm* phase (Fig. 1d-e). This phase also gives rise to superlattice reflections, revealing a superstructure with k = (1/2, 0, 0), which we designate as the Charge-Ordered-I phase (C-O-I; evidence for charge ordering is presented in the following section). The new phase progressively dominates with increasing pressure (Extended Data Fig. 1a) and above 50 GPa, its structure is resolved in a monoclinic $P2/c$ space group (no. 13; Extended Data Table 1, Supplementary Data 2), characterized by a doubling of the periodicity along the *a*-axis relative to the *Cmcm* phase.

At 54(1) GPa, another charge-ordered phase emerges with the monoclinic $P2/c$ space group (C-O-II; Fig. 1a; Extended Data Table 1; Supplementary Data 3), characterized by an additional doubling of the periodicity along the *c*-axis and an ordering vector k = (1/2, 0, 1/2) (Fig. 1f-g). In contrast to the onset of C-O-I, we observe no coexistence of C-O-II with the preceding phase. The C-O-II superlattice reflections disappear above 60(1) GPa (Fig. 1h-i; Extended Data Fig. 2), and Fe_4O_5 adopts a monoclinic $C2/m$ structure (no. 12; Supplementary Data 4), with the unit cell of the same size as the ambient-pressure *Cmcm* phase, i.e. k = (0, 0, 0).

Remarkably, further compression above 81(1) GPa re-establishes charge ordering in a third charge-ordered phase with a triclinic $P\bar{1}$ structure (no. 2; C-O-III; Fig. 1a, j-k) characterized by a different ordering vector k = (1/4, 1/4, 0). Owing to the limited diffraction data quality in the Diamond Anvil Cell, the C-O-III structure was analyzed using a $P2_1/n$ structural model; further details are provided in Extended Data Fig. 3 and Supplementary Data 5. Above 97(1) GPa, Fe_4O_5 reverts to the same charge-disordered monoclinic $C2/m$ phase, which persists up to the highest investigated pressure of 109(2) GPa (Fig. 1a, l-m).

In total, Fe_4O_5 adopts four previously unreported phases at the pressure above 38(1) GPa: three charge-ordered phases and one disordered phase (Fig. 1a). These superstructures are easily overlooked: the satellite reflections are far weaker than the fundamental ones (detailed in Methods), making their observation critically dependent on crystal quality, which deteriorates with increasing pressure and across successive phase transitions. In the previous room-temperature study no symmetry lowering was reported up to ~ 100 GPa (ref.[21]), consistent with the reduced quality of their single-crystal data upon compression. In contrast to the crystals synthesized *in situ* that were used above ~ 50 GPa in ref. [21], the single-crystal X-ray diffraction data reported here were collected from a pre-synthesized high-quality single crystal in one experimental run (Methods). Notably, the pressure boundaries of all three charge-ordered phases coincide with octahedral spin crossovers, previously reported in this compound[20–22] (Fig. 1a), a relation we establish in the next section.

Site-resolved charge and spin states

To follow the structural and electronic evolution across the pressure-induced phase transitions, we combined synchrotron Mössbauer source (SMS) spectroscopy measurements (Fig. 2) and single-crystal X-ray diffraction (XRD) structure refinements (Fig. 3). All structural phase transitions here are of the displacive type, we, therefore, also implemented a symmetry-mode analysis[24] (Extended Data Fig. 3; Extended Data Table 2), which decomposes each distorted structure into symmetry-adapted modes of the parent structure, labelled by irreducible representations of *Cmcm*. This allows the phases to be compared directly in terms of which distortions are active in each, rather than through their individual atomic coordinates, and provides a common framework for rationalizing the phase diagram.

The parent *Cmcm* structure contains three distinct crystallographic iron sites: one prismatic Fe1 site at the 4*c* position and two crystallographically distinct octahedral sites - Fe2 at 4*a* and Fe3 at 8*f* sites (refs.[7,19]; Supplementary Data 1). SMS spectra confirm that the *Cmcm* phase contains a magnetic sextet from the mixed-valent octahedral Fe2 and Fe3 sites and a paramagnetic doublet from Fe^{2+} on the prismatic Fe1 site (Fig. 2a; Extended Data Table 3; refs[22,23,25]). Both components remain essentially unchanged up to the onset of C-O-I at 38(1) GPa (Extended Data Fig. 1b), consistent with the persistence of the *Cmcm* phase established by XRD.

The symmetry reduction from *Cmcm* to the C-O-I structure allows several distortion modes, of which only Σ_2 and Γ_3^+ refine to significant amplitudes (Extended Data Fig. 3; Extended Data Table 2). The Σ_2 distortion dimerizes the octahedrally coordinated Fe sublattice along the *a*-axis (Fig. 3b-c), while Γ_3^+ produces a small monoclinic distortion. Both the Fe2 single chains and Fe3 double chains develop alternating Fe-Fe separations with short intradimer contact of ~ 2.56 Å and the corresponding interdimer separations substantially larger at ~ 2.77 Å at 51.6(10) GPa, whereas the trigonal-prismatic Fe1 sites remain undimerized.

The formation of C-O-I coincides with the appearance of a non-magnetic singlet (Fig. 2b; Extended Data Fig. 1b), characteristic of low-spin mixed-valence Fe in octahedral coordination[26,27], and previously observed around 55 GPa (ref. [22]). Its abundance is small, as expected at the onset of the crossover (Extended Data Fig. 1). The structure refinement places the crossover on the Fe2 site whose average Fe-O bond lengths shorten (Fig. 4a), consistent with the onset of the volume collapse (Extended Data Fig. 4) expected for a high-spin to low-spin transition[21]. Thus, the C-O-I phase hosts a mixed-spin state on the Fe2 site.

The octahedral sublattice of C-O-I contributes spectral components with distinct centre shifts, spanning values characteristic of nearly Fe^{3+} to intermediate valence (Extended Data Table 3). This differentiation of the octahedral iron into inequivalent, charge-localized environments, identifies C-O-I as a charge-ordered phase. Spin-state ordering (refs. [14,16–18]) can account neither for this valence differentiation nor for a superstructure that is present from the onset of C-O-I, where the low-spin fraction is still minimal (Fig. 4b). The same holds at the onset of C-O-III, when the low-spin fraction on Fe3 is still minimal (please see below and Fig. 4b).

The C-O-II structure observed between 54(1)-60(1) GPa is not a subgroup of C-O-I, precluding a continuous transition between the two phases and indicating that the transition is first order (Extended Data Fig. 3). C-O-II largely retains the dimerized framework of C-O-I but is distinguished by the condensation of an additional A_1 mode with k = (1/2, 0, 1/2) (Extended Data Table 2). This mode doubles the periodicity along the *c* axis, a feature not observed in previously reported charge-ordered phases of Fe_4O_5 (refs. [7,23]). Dimerization becomes partial in C-O-II: within both the Fe2 and Fe3 chains, some sites remain paired whereas others are no longer dimerized. The trigonal-prismatic Fe1 chains develop a weak alternation of Fe-Fe separations (Fig. 3d-f), but its amplitude is smaller by an order of magnitude smaller than the dimerization of the octahedral chains. This weaker displacement suggests that prismatic sublattice does not itself develop dimers. Instead, the Fe1 sites evolve from predominantly Fe^{2+} in C-O-I phase towards a mixed-valence state close to $Fe^{2.5+}$ in C-O-II phase (Fig. 2c; Extended Data Table 3), transferring charge to the octahedral network and thereby altering its average valence. The evolution of the prismatic Fe1 valence parallels the pressure-driven electron transfer from the prismatic to the octahedral chains proposed for the low-temperature phases (ref. [23]).

Most of the Fe2 crossover takes place within C-O-II. The relative abundance of the low-spin singlet continues to grow and a low-spin Fe^{3+} doublet appears in the SMS spectra (Figs. 2c and 4b), and the corresponding Fe-O bonds contract progressively (Fig. 4a). As in C-O-I, a charge-localized Fe^{3+} component coexists with intermediate-valence components (Extended Data Table 3). Together with the associated superstructure, this valence differentiation identifies C-O-II as a charge-ordered phase.

Above 60(1) GPa, the transition to the monoclinic *C*2/*m* phase largely restores the parent symmetry. The superstructure disappears and the unit cell returns to that of the parent *Cmcm* phase (Fig. 1h-i; Extended Data Table 1). Only the Γ_3^+ distortion remains active, with a substantially reduced amplitude (Extended Data Table 2). The relative abundance of low-spin octahedral iron reaches a plateau in the 60(1)-81(1) GPa pressure range (Fig. 4b), marking completion of the spin crossover at the octahedral Fe2 sites. The disappearance of charge ordering thus coincides with the completion of the Fe2 crossover. The *C*2/*m* phase contains both spin states, but they occupy different crystallographic sites: Fe2 is low spin, whereas Fe3 remains high spin, and no charge ordering is observed (Fig. 2d).

Charge ordering re-emerges above 81(1) GPa in the C-O-III phase, which is primarily described by S_1^+ and P_2 distortion modes (Extended Data Table 2; Extended Data Fig. 3), where the P_2 mode produces substantial distortions of the trigonal-prismatic Fe1 chains. Unlike the preceding charge-ordered phases, C-O-III no longer contains linear Fe dimers. Instead, the Fe atoms assemble into isolated planar bent trimers composed of one Fe2 ion and two Fe3 ions (Fig. 3g; Extended Data Fig. 5). Resistance measurements indicate an insulator-to-metal transition near 84 GPa (ref.[21]), placing C-O-III in a metallic regime. The persistence of Verwey-type charge ordering under these conditions is unusual, as metallization would normally favour electron delocalization[28]. This coexistence can be rationalized by the separation of localized and itinerant electronic states: electrons involved in trimer formation remain confined within finite Fe clusters, whereas carriers on the remaining Fe sublattices sustain metallic transport. C-O-III therefore represents an unusual spin-crossover-stabilized metallic charge-ordered state in a mixed-valence oxide.

In the SMS spectra of the C-O-III phase (Fig. 2e) the prismatic Fe1 chains show distinct Fe^{2+} and Fe^{3+} components rather than the mixed-valence configuration observed in *C2/m* (Extended Data Table 3), which together with the superstructure identifies C-O-III as charge-ordered. For the prismatic sites, DFT+DMFT predicts a valence change from Fe^{2+} to Fe^{3+} change above ~ 84 GPa (ref.[21]). We observe instead a change to mixed valence already from 54(1) GPa in the C-O-II phase, which near the predicted pressure splits into distinct Fe^{2+} and Fe^{3+} in the C-O-III phase. Concurrently, the relative abundances of low-spin octahedral iron increase sharply at the expense of the corresponding high-spin component (Fig. 4b), marking the onset of spin crossover on octahedral Fe3 sites (Fig. 4a), while the Fe2 sites remain fully in the low-spin state. The crossover is completed at 97(1) GPa (Fig. 4), coinciding with the disappearance of the C-O-III phase and recovery of the charge-disordered *C*2/*m* structure (Fig. 1l-m). The Fe1 sites revert to the mixed-valence state in *C*2/*m* (Fig. 2f; Table 2) with no qualitative change observed upon further compression up to 112(3) GPa.

Taken together, the two charge-ordering episodes follow the same sequence. Charge order sets in when the spin crossover begins on one octahedral site, persists while high-spin and low-spin Fe coexist on that site, and disappears once the crossover there is complete: at 38(1)–60(1) GPa for Fe2 and at 81(1)–97(1) GPa for Fe3. Above 97(1) GPa both octahedral sites are fully low-spin, and no further charge ordering occurs. None of the phases reported here corresponds to the low-temperature charge-ordered phases of Fe_4O_5 (refs[7,23]), which have different symmetries and propagation vectors, nor to the dimerized Fe_4O_5-IV obtained by laser heating at 45 GPa ($P2_1/m$, with dimerized prismatic chains; ref. [23]).

Spin-state heterogeneity and pressure-induced charge order

Charge order in Fe_4O_5 is thus confined to the mixed-spin regimes of the octahedral Fe2 and Fe3 sites, separated by 40 GPa (Fig. 4). Below 38(1) GPa, compression alone leaves the charge-averaged *Cmcm* structure intact. These observations argue that the pressure-induced spin crossover in Fe_4O_5 drives the charge ordering rather than the reverse: calculations within the parent *Cmcm* structure reproduce the sequence of the crossovers without any charge order[20–22], whereas experimentally charge ordering emerges only while a crossover is underway. The reverse, a spin-state transition induced by charge ordering, has been reported in the layered cobaltite $YBaCo_2O_5$ (ref. [10]). Coexistence of the two spin states alone, however, is not sufficient. Between 60(1) and 81(1) GPa in the *C*2/*m* phase, high-spin Fe3 and low-spin Fe2 coexist but are segregated onto crystallographically distinct sites, and no charge order is observed. Nor is spin-state heterogeneity on a single site sufficient: e.g., in $FeBO_3$, high- and low-spin Fe^{3+} coexist on one crystallographic site over about 50 GPa without any superstructure[29]. Pressure-induced charge order in Fe_4O_5 thus requires both spin-state heterogeneity within a single site and a mixed valence that supplies charge to localize.

We propose that the crossover enhances the coupling between charge and lattice degrees of freedom. Within the mixed-spin regime, high- and low-spin states on the same site are close in energy. This makes the local spin state, and hence ionic size, highly sensitive to small changes in electron occupancy or structural distortion. At the same time, upon the crossover, the lattice softens[21,29,30], lowering the elastic cost of a cooperative distortion. Both effects favour localizing charge in distorted Fe-Fe units over the charge-averaged state that compression otherwise promotes by broadening the Fe 3*d* bands. In this picture, what matters is that a site is in its mixed-spin regime, not how many of its ions are low-spin. In Fe_4O_5, this accounts for charge order appearing even when only a few per cent of the octahedral iron is low-spin (C-O-I; Fig. 4b), and for its disappearance once each crossover is complete. Model calculations point the same way: near spin-state degeneracy, both electronic[31] and elastic[16] interactions favour symmetry-broken states, whereas this tendency weakens away from degeneracy. Spin crossover therefore provides a route to charge order that differs from that in magnetite[3,28,32]. Fe_4O_5 hosts both routes: at low temperature, charge order develops without a spin crossover[7,23], and at room temperature compression promotes the spin-crossover-mediated route.

The structural motif of the charge order changes with the site undergoing the crossover. In C-O-I, both octahedral chains are fully dimerized, while in C-O-II, both retain dimers but neither remains fully dimerized (Fig. 3). In C-O-III, the dimers are replaced by isolated, planar bent trimers, each comprising one low-spin Fe2 and two Fe3 ions (Fig. 3; Extended Data Fig. 5), with Fe3 being the site undergoing the crossover (Fig. 4). Trimer formation is accompanied by a reduction of the Fe2-O-Fe3 angle well below 90°, compared with values close to 90° in all other phases. This geometry shortens the Fe2-Fe3 contacts and enhance direct overlap of Fe 3*d* orbitals, characteristic ingredient of orbital-molecule formation (refs. [33,34]). Trimers also occur in magnetite (ref. [3]), $CaFe_3O_5$ (refs. [35,36]) and low-temperature phases of Fe_4O_5 (refs. [7,23]), but are linear in all of these iron oxides. Planar trimers are known in other transition-metal oxides, such as $LiVO_2$ (ref. [33]), and CsW_2O_6 (ref. [34]), but have no precedent in iron oxides. Moreover, unlike these previously known planar trimers, those in Fe_4O_5 are open and emerge only within the spin-crossover regime.

The two conditions identified here, mixed valence and a spin crossover occurring within a single crystallographic site, are not unique to Fe_4O_5. Other mixed-valence oxides, such as Fe_5O_6 (refs. [8,37,38]), $CaFe_3O_5$ (refs. [35,36]), and $LuFe_2O_4$ (ref. [6]) are natural candidates to test this mechanism under compression. More broadly, our results establish spin crossover as a previously unrecognized route to charge order in mixed-valence oxides, and suggest that controlled access to mixed-spin states, through pressure[4], temperature[14] or light[15,39], could provide a means to create and tune charge order in correlated transition-metal oxides.

Methods

Sample synthesis

Samples of $^{57}Fe_4O_5$ were synthesized from stoichiometric mixtures of fine $^{57}Fe_2O_3$ and ^{57}Fe powders using 1,200-ton multi-anvil presses[40] at the Institute of Mineralogy, University of Münster, Germany, and at the Synergetic Extreme Condition User Facility (SECUF), Jilin University, China, following established procedures[7,23]. The syntheses were performed at a pressure of 11 GPa and temperature of 1350 °C over 6 hours. We employed a standard assembly including an Au cylindrical sample capsule, a $LaCrO_3$ heater, a W3Re/W25Re thermocouple, and other components packed inside an octahedron made of Cr-bearing MgO. About 100 synthesized crystals were preselected by single crystal X-ray diffraction at ID15b and Synchrotron Mössbauer Source (SMS) spectroscopy at ID18 (currently ID14), ESRF. The crystals with the best quality were chosen for loadings.

High-pressure experiments

High-pressure experiments were conducted using membrane-type diamond anvil cells[41]. Diamonds with 150 μm culets were used to achieve pressures up to 112 GPa. Compression chambers were prepared

from 200 μm-thick Re gaskets, pre-indented to approximately 30 μm thickness and laser-drilled with 75 μm holes. The pre-selected crystals (each about 15 × 15 × 10 μm^3 in size) were loaded into the pressure chamber, together with Ne that was loaded at 1.2 kbar and served as a pressure-transmitting medium. Pressure was determined from gold and ruby, loaded in the chamber in XRD and SMS experiments, respectively[42,43]. Uncertainties of individual pressures reflect those of the respective calibrant. Uncertainties in phase boundaries reflect the difference between the two pressure scales. All measurements were performed at room temperature.

Synchrotron X-ray diffraction experiments

The single-crystal XRD experiments were conducted at the ID15b beamline[44] (MAR555 detector, wavelength λ = 0.4100 Å) of the European synchrotron radiation facility (ESRF), Grenoble, France. The X-ray spot size was around 1 μm. Single-crystal datasets were collected via rotation of the DAC around the ω axis from − 30° to 30° with an angular step of 0.5°. Integration of the reflection intensities and absorption corrections were performed using CrysAlisPro software. The satellite reflections of the charge-ordered phases are much weaker than the fundamental ones: the mean I/σ of satellite reflections is typically two orders of magnitude lower than that of fundamental reflections. Their detection therefore depends critically on crystal quality. The structures were solved by the direct method and refined in the isotropic approximation by full-matrix least-squares refinements using SHELXS and SHELXL software in OLEX2[45,46], respectively. Because all transitions are displacive, each distorted structure was described by symmetry-adapted modes of the parent *Cmcm* structure, allowing the phases to be compared through their active distortions rather than individual atomic coordinates. The modes were generated with ISOTROPY[47], and their amplitudes were refined with FULLPROF[48]. Note that the single-crystal XRD data reported here were collected in one experimental run, i.e. all XRD data correspond to the same single crystal of Fe_4O_5, compressed to 109 GPa.

Mössbauer spectroscopy under extreme conditions

SMS spectra were recorded at the Nuclear Resonance Beamline ID18 (currently ID14) of the ESRF using the (111) nuclear reflection of a $^{57}FeBO_3$ single crystal mounted on a Wissel velocity transducer driven with a sinusoidal wave form[49,50]. The source provides ^{57}Fe resonant radiation at 14.4 keV within a bandwidth of 15 neV (0.31 mm/s) which is tunable in energy. The X-ray beam was focused down to 13 × 4 μm^2 (vertical × horizontal) with Kirkpatrick-Baez mirrors. The linewidth of the SMS and the absolute position of the centre shift (CS) relative to α-Fe were controlled before and after each measurement with a $K_2Mg^{57}Fe(CN)_6$ reference single-line absorber. The velocity scale was calibrated using 25-μm-thick natural alfa iron foil. SMS spectra were fitted using the full transmission integral taking into account the exact shape of the SMS instrumental function. The fitting procedure was done in SYNCmoss software[51].

Spin and valence states were assigned from the centre shift and the hyperfine magnetic field, taking into account their pressure dependence in reference iron oxides[13,27]. Low-spin components were identified by their characteristic low CS together with the abrupt loss of magnetic hyperfine splitting. For intermediate components, the valence was estimated by interpolating between the values expected for Fe^{2+} and Fe^{3+} at a given pressure.

Relative abundances were obtained assuming equal Lamb–Mössbauer factors for all components. This assumption introduces systematic deviations: the larger, less rigid sites are expected to have a lower Lamb–Mössbauer factor whereas the smaller and stiffer sites are expected to have a higher one. This results in an underestimation of the relative abundance of the prismatic spectral components and an overestimation for the low-spin components. In the coexistence region, low-spin abundances in C-O-I were normalized to the C-O-I phase fraction, which was obtained from the relative abundances of the prismatic components of C-O-I and *Cmcm*.

Declarations

Acknowledgements

We acknowledge the European Synchrotron Radiation Facility (ESRF) for provision of synchrotron radiation facilities under proposal number ES-1186 at ID18 and ID15b beamlines. We also acknowledge the Sample Environment Service-HP lab and J. Jacobs for technical support of the loan pool diamond anvil cells. This work was supported by the Synergetic Extreme Condition User Facility (SECUF)- Jilin Branch and Instrument and Equipment Sharing Platform, State Key Laboratory of High Pressure and Superhard Materials, Jilin university. The authors thank Qian Cheng and Lianjie Man for the discussion and help of the sample synthesis. X. Li and I. Kupenko thank the German Research Foundation (Deutsche Forschungsgemeinschaft, DFG, Project AOBJ: 674300 GZ: KU 3832/3-1) for funding.

Data availability

Crystallographic data for the structures reported are as the Supplementally Data 1-5.

Author Contributions

X.L. and I.K. initiated and designed the research. X.L., H.T., A.L., P.P., A.R., S.K., and L.D. synthesized the samples. The SMS data were collected by X.L., D.V., G.A., S.M, S,Y., E.Klyushina., O.S., E.Blackburn., A.C., C.S.V. and I.K. X.L., E.Bykova., M.B., E.Kolesnikov., D.C., and M.H. performed the single-crystal X-ray diffraction. X.L., D.V., M.B., and I.K. interpreted the data. X.L. wrote a draft of the manuscript, and all the co-authors read, revised and commented on it.

Conflict of interest

The Authors declare no competing interests.

References

1. Verwey EJW (1939) Electronic conduction of magnetite (Fe_3O_4) and its transition point at low temperatures. Nature 144:327–328
2. Attfield J, Bell A, Rodriguez-Martinez L et al (1998) Electrostatically driven charge-ordering in Fe_2OBO_3. Nature 396:655–658
3. Senn MS, Wright JP, Attfield JP (2012) Charge order and three-site distortions in the Verwey structure of magnetite. Nature 481:173–176
4. Kawakami T et al (2009) Spin transition in a four-coordinate iron oxide. Nat Chem 1:371–376
5. Teng X et al (2022) Discovery of charge density wave in a kagome lattice antiferromagnet. Nature 609:490–495
6. Ikeda N et al (2005) Ferroelectricity from iron valence ordering in the charge-frustrated system $LuFe_2O_4$. Nature 436:1136–1138
7. Ovsyannikov SV et al (2016) Charge-ordering transition in iron oxide Fe_4O_5 involving competing dimer and trimer formation. Nat Chem 8:501–508
8. Ovsyannikov SV et al (2020) A Room-Temperature Verwey-type Transition in Iron Oxide, Fe_5O_6. Angew Chem Int Ed Engl 59:5632–5636
9. Renner CH, Aeppli G, Kim BG, Soh YA, Cheong SW (2002) Atomic-scale images of charge ordering in a mixed-valence manganite. Nature 416:518–521
10. Vogt T et al (2000) Low to high spin-state transition induced by charge ordering in antiferromagnetic $YBaCo_2O_5$. Phys Rev Lett 84:2969–2972
11. Cohen RE, Mazin II, Isaak DG (1997) Magnetic collapse in transition metal oxides at high pressure: implications for the Earth. Science 275:654–657
12. Lin JF et al (2005) Spin transition of iron in magnesiowustite in the Earth's lower mantle. Nature 436:377–380
13. Vasiukov DM et al (2017) Pressure-induced spin pairing transition of Fe^{3+} in oxygen octahedra. https://arxiv.org/abs/1710.03192
14. Shatruk M, Phan H, Chrisostomo BA, Suleimenova A (2015) Symmetry-breaking structural phase transitions in spin crossover complexes. Coord Chem Rev 289–290:62–73
15. Ohkoshi S, Imoto K, Tsunobuchi Y, Takano S, Tokoro H (2011) Light-induced spin-crossover magnet. Nat Chem 3:564–569
16. Khomskii DI, Löw U (2004) Superstructures at low spin–high spin transitions. Phys Rev B 69:184401
17. Collet E et al (2012) Aperiodic spin state ordering of bistable molecules and its photoinduced erasing. Phys Rev Lett 109:257206
18. Granado E, Galdino CW, Moreno BD, King G, Freitas DC (2024) Spin-state ordering and intermediate states in the mixed-valence cobalt oxyborate $Co_3O_2BO_3$ with spin crossover. Phys Rev B 109:094115

19. Lavina B et al (2011) Discovery of the recoverable high-pressure iron oxide Fe_4O_5. Proc Natl Acad Sci U S A 108:17281–17285
20. Yang A et al (2021) Metallic nature and site-selective magnetic moment collapse in iron oxide Fe_4O_5 at the extreme conditions of Earth's deep interior. Phys Lett A 414:127607
21. Layek S et al (2022) Verwey-Type Charge Ordering and Site-Selective Mott Transition in Fe_4O_5 under Pressure. J Am Chem Soc 144:10259–10269
22. Zhandun VS et al (2024) Orthogonal magnetic structures of Fe_4O_5: representation analysis and DFT calculations. Dalton Trans 53:2242–2251
23. Ovsyannikov SV et al (2018) Pressure tuning of charge ordering in iron oxide. Nat Commun 9:4142
24. Perez-Mato JM, Orobengoa D, Aroyo M (2010) I. Mode crystallography of distorted structures. Acta Crystallogr A 66:558–590
25. Vasiukov DM et al (2022) Symmetry protected 1D chains in mixed-valence iron oxides. arXiv preprint arXiv :220714111
26. Pasternak MP et al (1997) High pressure collapse of magnetism in $Fe_{0.94}O$: Mössbauer spectroscopy beyond 100 GPa. Phys Rev Lett 79:5046
27. Li X et al (2024) Monoclinic distortion and magnetic transitions in FeO under pressure and temperature. Commun Phys 7:305
28. Rozenberg G et al (2006) Origin of the Verwey transition in magnetite. Phys Rev Lett 96:045705
29. Xu W et al (2022) Pressure-induced high-spin/low-spin disproportionated state in the Mott insulator $FeBO_3$. Sci Rep 12:9647
30. Lin J-F et al (2006) Pressure-induced electronic spin transition of iron in magnesiowustite-(Mg,Fe)O. Phys Rev B 73:113107
31. Kunes J, Krapek V (2011) Disproportionation and metallization at low-spin to high-spin transition in multiorbital Mott systems. Phys Rev Lett 106:256401
32. Wang W et al (2023) Verwey transitionas evolutionfrom electronicnematicityto trimerons via electron-phononcoupling. Sci Adv 9:23
33. Pen HF et al (1997) Orbital Ordering in a Two-Dimensional Triangular Lattice. Phys Rev Lett 78:1323
34. Okamoto Y et al (2020) Regular-triangle trimer and charge order preserving the Anderson condition in the pyrochlore structure of CsW_2O_6. Nat Commun 11:3144
35. Hong KH, Arevalo-Lopez AM, Cumby J, Ritter C, Attfield JP (2018) Long range electronic phase separation in $CaFe_3O_5$. Nat Commun 9:2975
36. Cassidy SJ, Orlandi F, Manuel P, Clarke SJ (2019) Single phase charge ordered stoichiometric $CaFe_3O_5$ with commensurate and incommensurate trimeron ordering. Nat Commun 10:5475
37. Lavina B, Meng Y (2015) Unraveling the complexity of iron oxides at high pressure and temperature: Synthesis of Fe_5O_6. Sci Adv 1:5

38. Qin Q-Y et al (2021) Site-Selective Magnetic Moment Collapse in Compressed Fe_5O_6. Chin Phys Lett 38:089101
39. Gütlich P, Garcia Y, Goodwin HA (2000) Spin crossover phenomena in Fe(II) complexes. Chem Soc Rev 29:419–427
40. Wijbrans CH, Rohrbach A, Klemme S (2016) An experimental investigation of the stability of majoritic garnet in the Earth's mantle and an improved majorite geobarometer. Contrib Mineral Petrol 171:5
41. Letoullec R, Pinceaux J, Loubeyre P, J. I. (1988) J. o. H. P. R. The membrane diamond anvil cell: a new device for generating continuous pressure and temperature variations. High Press Res 1:77–90
42. Fei Y et al (2007) Toward an internally consistent pressure scale. Proc Natl Acad Sci U S A 104:9182–9186
43. Shen G et al (2020) Toward an international practical pressure scale: A proposal for an IPPS ruby gauge (IPPS-Ruby2020). High Press Res 40:299–314
44. Garbarino G et al (2024) Extreme conditions X-ray diffraction and imaging beamline ID15B on the ESRF extremely brilliant source. High Press Res 44:199–216
45. Sheldrick GM (2008) A short history of SHELX. Acta Crystallogr A 64:112–122
46. Dolomanov OV, Bourhis LJ, Gildea RJ, Howard JAK, Puschmann H (2009) OLEX2: a complete structure solution, refinement and analysis program. J Appl Crystallogr 42:339–341
47. Campbell BJ, Stokes HT, Tanner DE, Hatch D (2006) M. ISODISPLACE: a web-based tool for exploring structural distortions. J Appl Crystallogr 39:607–614
48. Rodriguez-Carvajal J (1993) Recent advances in magnetic structure determination neutron powder diffraction. Phys B Condens Matter 192:55–69
49. Potapkin V et al (2012) The ^{57}Fe Synchrotron Mossbauer Source at the ESRF. J Synchrotron Radiat 19:559–569
50. Potapkin V et al (2012) The ^{57}Fe Synchrotron Mossbauer Source at the ESRF. J Synchrotron Radiat 19:559–569
51. Yaroslavtsev S (2023) SYNCmoss software package for fitting Mossbauer spectra measured with a synchrotron Mossbauer source. J Synchrotron Radiat 30:596–604

Figures

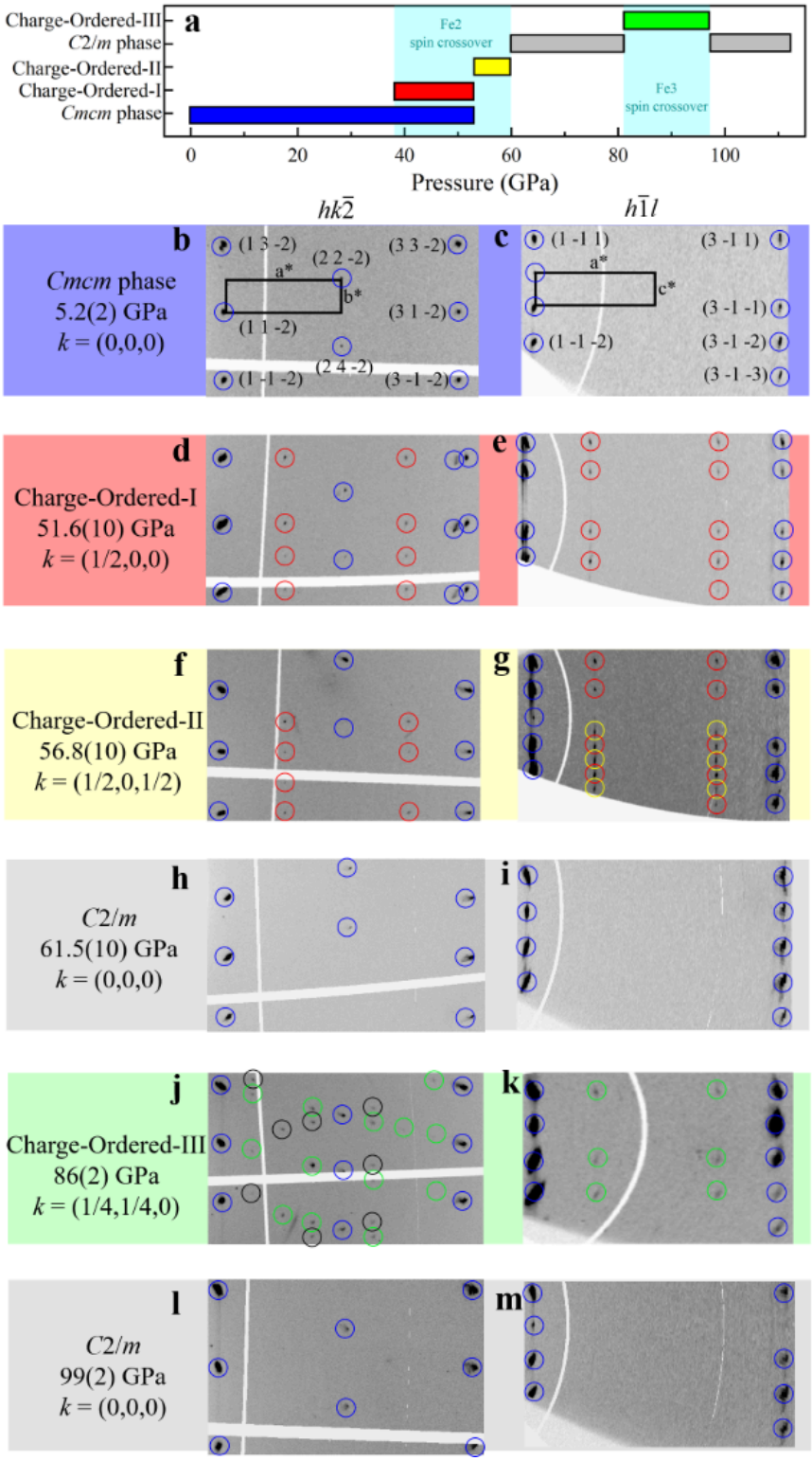


Figure 1

Pressure-induced structural transformations and superstructures in Fe_4O_5. a, Pressure ranges of the observed Fe_4O_5 phases up to 112 GPa. Cyan shadings mark the spin-crossover intervals of the octahedral Fe2 (38(1)–60(1) GPa) and Fe3 (81(1)–97(1) GPa) sites. **b-m,** Selected *hk* and *hl* reciprocal-lattice planes, indexed in the parent *Cmcm* cell, at indicated pressures. *k* denotes the corresponding propagation vectors. Blue circles are fundamental reflections common to all phases; red are superlattice

reflections from doubling of a; yellow are from doubling of c; green are superlattice reflections of C-O-III; black are reflections of a twin domain. **b-c**, *Cmcm* parent phase; a*, b*, and c* are reciprocal axes, with the same orientation in all panels. **d-e**, C-O-I; split fundamental reflections indicate coexisting *Cmcm* phase. **f-g**, C-O-II; reflections of *Cmcm* no longer observed, and diffuse scattering along c* is visible in **g** (its analysis is beyond the scope of this work). **h-i**, *C*2/*m*; superlattice reflections absent. **j-k**, C-O-III. **l-m**, recovery of *C*2/*m* phase.

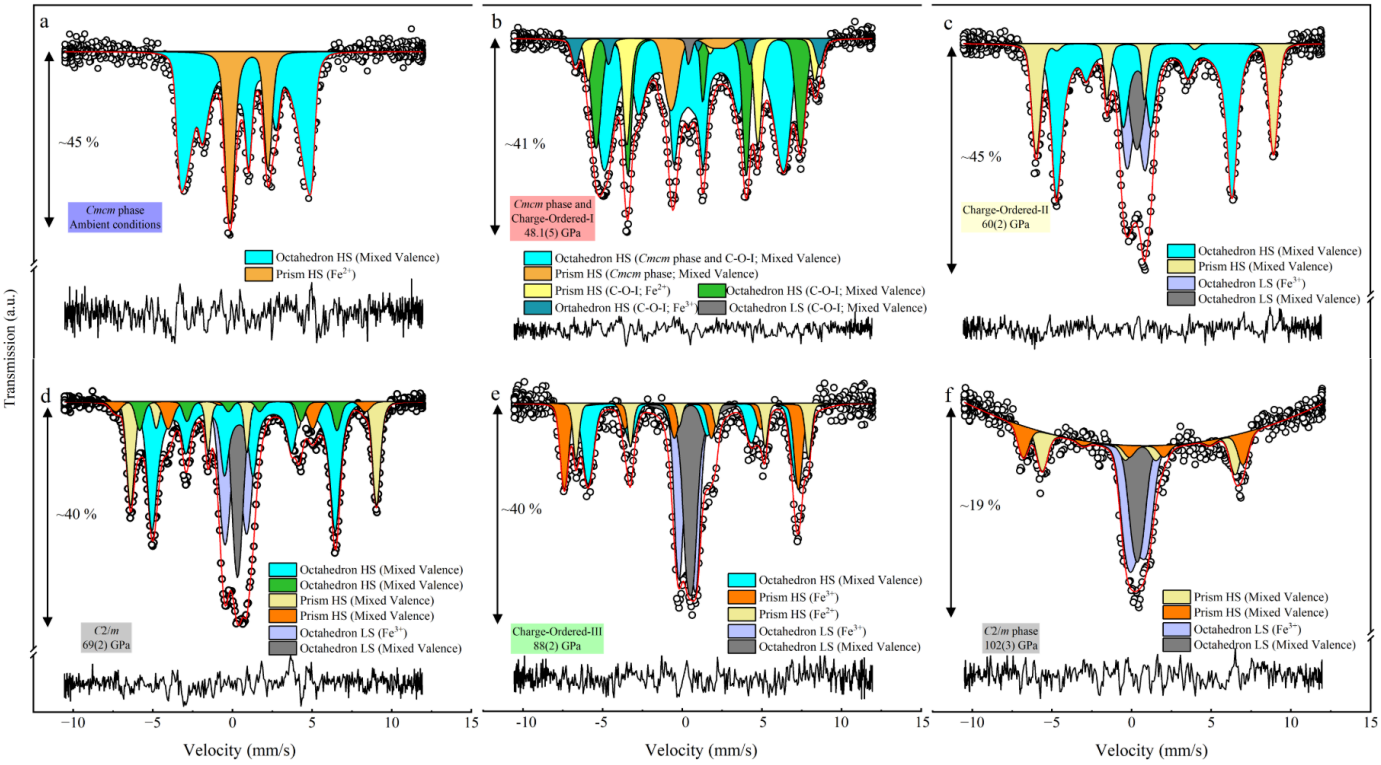


Figure 2

Evolution of the Fe electronic states across the pressure-induced phases of Fe_4O_5. **S**elected SMS spectra at the indicated pressures and room temperature. **a**, *Cmcm* phase at ambient conditions: a magnetic sextet from high-spin mixed-valence $Fe^{2.67+}$ component of the octahedral Fe2 and Fe3 sites, and a paramagnetic doublet from high-spin Fe^{2+} on the prismatic Fe1 site. **b**, Coexisting *Cmcm* and Charge-Ordered-I phases. The Charge-Ordered-I phase contributes a high-spin Fe^{2+} magnetic sextet from prismatic Fe1, octahedral high-spin sextets with distinct centre shifts, and a low-spin singlet from octahedral Fe2. The prismatic component of *Cmcm* shows the onset of magnetic ordering. **c**, Charge-Ordered-II phase: the *Cmcm* components have disappeared, prismatic Fe1 gives a single mixed-valence component, and a low-spin Fe^{3+} doublet appears alongside the low-spin singlet. **d**, Charge-disordered *C*2/*m* phase, with low-spin iron on the Fe2 sites and high-spin iron on Fe3 sites. **e**, Charge-Ordered-III phase: prismatic Fe1 is split into distinct high-spin Fe^{2+} and Fe^{3+} sextets. **f**, *C*2/*m* phase above 100 GPa. Red solid lines show the model fits, the percentage bars indicate the relative absorptions, and the

residuals of the fits are indicated below each spectrum. Hyperfine parameters are listed in Extended Data Table 3.

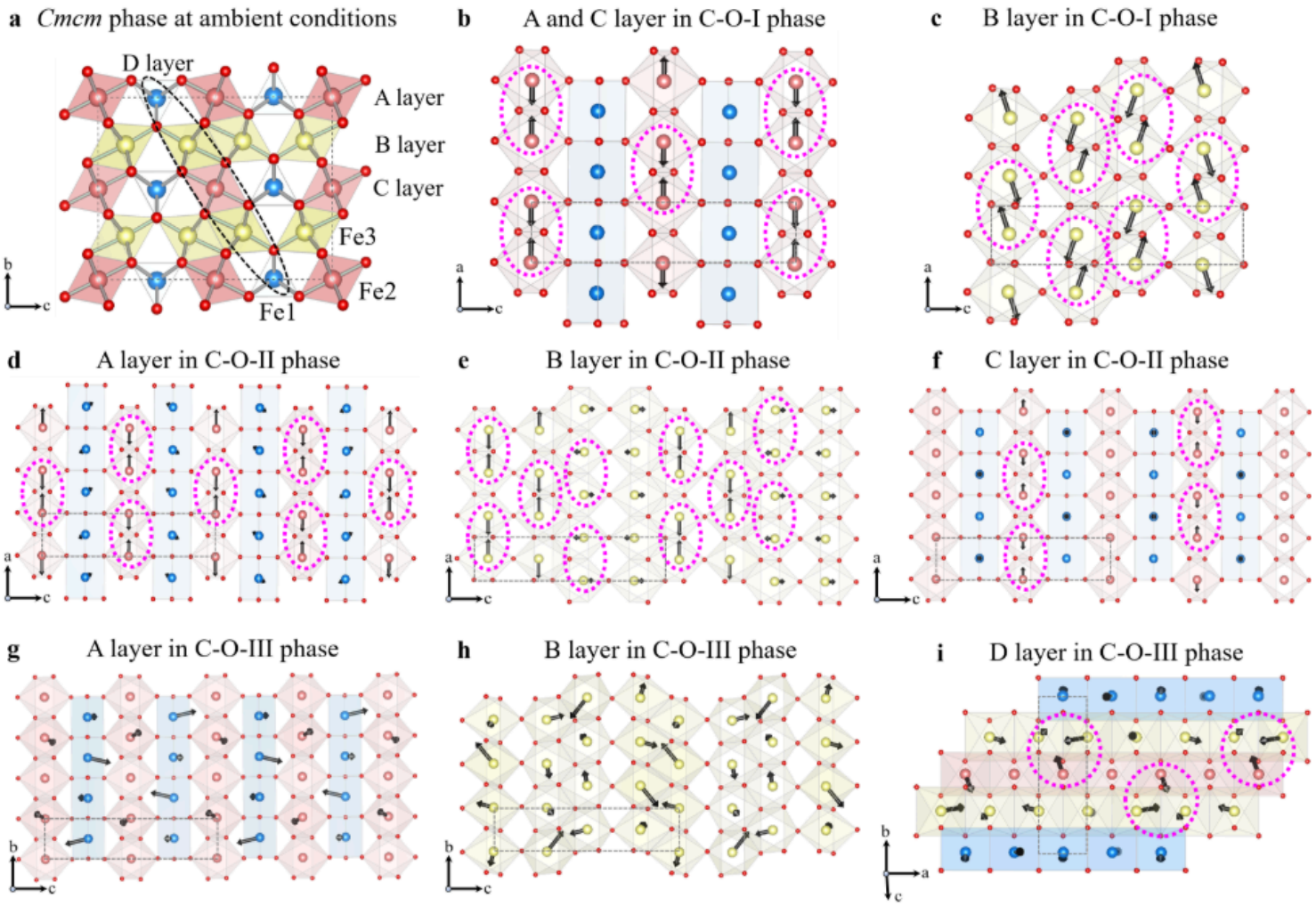


Figure 3

Evolution of structures of different Fe_4O_5 phases. Grey dashed rectangles outline the parent *Cmcm* unit cell. Crystallographic directions refer to the parent *Cmcm* setting. Blue, pink, and yellow spheres denote trigonal-prismatic Fe1 and octahedral Fe2 and Fe3 sites, respectively. Red spheres denote oxygen atoms Dashed purple circles show the dimers and trimers in the structures. **a**, Ambient-pressure *Cmcm* structure projected down the a-axis. **b-c**, Charge-Ordered-I structure: parent Fe2 and Fe3 sites split into symmetry-inequivalent positions, the octahedral chains dimerize along the a-axis. At 51.6(10) GPa, the Fe2 and Fe3 chains exhibit intradimer Fe-Fe distances of ~2.57 and ~2.55 Å, respectively, separated by interdimer contacts of ~2.76 and ~2.77 Å, whereas the alternation within trigonal-prismatic Fe1 chains is below 0.005 Å. **d-f**, Charge-Ordered-II structure: doubling of the periodicity along the *c* axis. Dimerization becomes partial in both the Fe2 and Fe3 chains, whereas the Fe1 chains develop only a weak alternation of Fe-Fe distances of ~2.64 Å and ~2.67 Å at 54.4(10) GPa. **g-i**, Charge-Ordered-III structure: isolated planar bent trimers, each of one Fe2 and two Fe3. The Fe1 chains develop alternating Fe–Fe distances of ~2.60 Å and ~2.63 Å at 86(2) GPa. Arrows denote the combined atomic displacements of iron atoms

relative to the parent structure; oxygen displacements are not shown. The symmetry-mode decomposition is given in Extended Data Table 2 and Extended Data Fig.3.

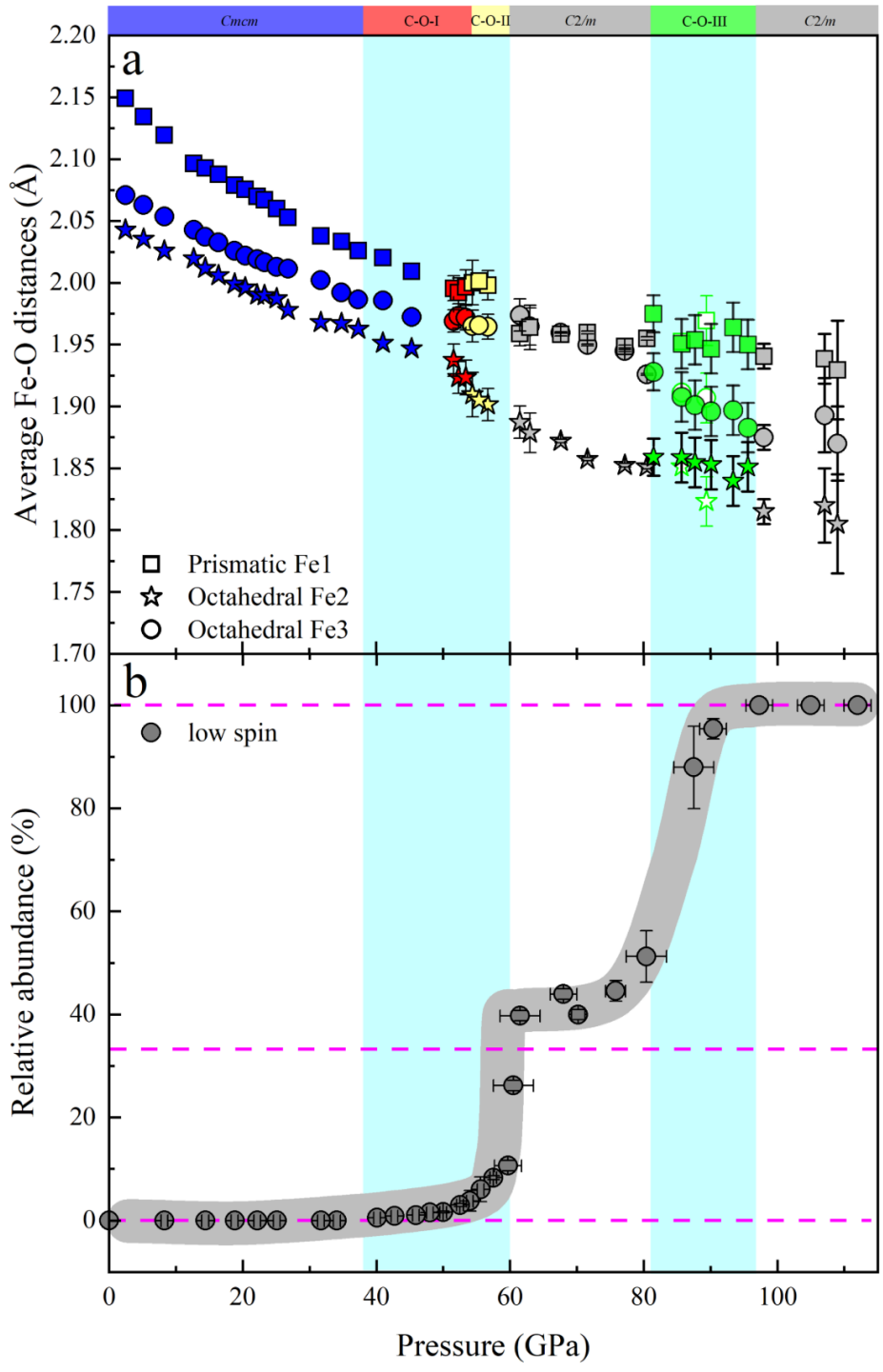


Figure 4

Pressure evolution of site-resolved Fe-O bond distances and spin states of octahedral Fe in Fe_4O_5. Charge-ordered phases occur exclusively within mixed-spin regimes (cyan shadings) in which one of the

octahedral Fe2 and Fe3 sites contains both high-spin and low-spin Fe. **a**, Average Fe-O bond distances for the trigonal-prismatic Fe1 and octahedral Fe2 and Fe3 sites. In the high-pressure phases, the parent Fe sites split into several symmetry-inequivalent positions, and each plotted value therefore represents an average over the corresponding split sites. Blue symbols denote the *Cmcm* phase. Within the *Cmcm*-Charge-Ordered-I coexistence region, blue and red symbols represent data refined using the *Cmcm* and C-O-I structural models, respectively. Grey symbols denote the *C*2/*m* phase, whereas solid green symbols denote the Charge-Ordered-III phase refined in the average *C*2/*m* structure, because the superstructure refinement is limited by the weak satellite reflections (Methods). Open green symbol show bond lengths obtained from direct refinement of the C-O-III structure, which are consistent with the *C*2/*m*-based values. C-O-I could not be refined below 50 GPa because of its small phase fraction. **b**, Relative abundances of low-spin Fe on the octahedral sites of Fe_4O_5. The trigonal-prismatic Fe1 sites (not shown) remain in the high-spin state at investigated pressures. Values for C-O-I are normalized to its phase fraction (Methods). Dashed lines mark 0%, 33% and 100%. The 33% line corresponds to a complete crossover of the Fe2 site, which holds one third of the octahedral iron. The plateau lies somewhat above it because the low-spin abundance is systematically overestimated (Methods).

Supplementary Files

This is a list of supplementary files associated with this preprint. Click to download.

- Extendeddatafiguresandtables.docx
- SupplementaryData1Fe4O5Cmcm5.2GPa.cif
- SupplementaryData4Fe4O5C2m60GPa.cif
- SupplementaryData3Fe4O5COII54.4GPa.cif
- SupplementaryData5Fe4O5COIII85.7GPa.cif
- SupplementaryData2Fe4O5COI51.6GPa.cif